nanomaterials

MDPI

Article

1T-ZrS_2 Monolayer Decorated with Sc, Ti, and V Single Atoms: A Potential Gas Scavenger for NO_x and SO_2

Xiaoxuan Wang [1,†], Jiaqi Zhang [1,†], Jinjuan Zhang [1,*], Xiaoqing Liu [2], Yuanqi Lin [1], Fangfang Li [1], Guangwei Wang [1,*], Yan Xu [1] and Peng Wang [1,*]

[1] College of Electronic and Information Engineering, Shandong University of Science and Technology, Qingdao 266590, China; 202482130011@sdust.edu.cn (X.W.); lifangfang@sdust.edu.cn (F.L.)
[2] School of Mathematical Sciences, Shanghai Jiao Tong University, Shanghai 200240, China; liuxiaoq1994@gmail.com
* Correspondence: zhangjinjuan@sdust.edu.cn (J.Z.); wanggw@sdust.edu.cn (G.W.); phywangp@sdust.edu.cn (P.W.)
† These authors contributed equally to this work.

Abstract

The intensification of industrialization and increasing energy consumption have led to elevated emissions of hazardous gases such as NO, NO_2, and SO_2, making their efficient capture and removal crucial for environmental remediation. In this work, first-principles calculations were employed to systematically investigate the adsorption behavior of these gases on single-atom-decorated (Sc, Ti, and V) 1T-ZrS_2 monolayers. The results indicate that the transition metal atoms preferentially occupy the hexagonal hollow sites of ZrS_2, forming an approximately octahedral coordination field and exhibiting characteristic *d*-orbital splitting. During gas adsorption, the decorated systems exhibit pronounced metal-to-adsorbate charge donation and strong *d-p* hybridization, indicative of strong chemisorption. Notably, Ti-ZrS_2 exhibits the strongest adsorption toward NO_2, inducing partial molecular dissociation and suggesting catalytic activity, whereas Sc- and V-decorated systems predominantly maintain molecular adsorption. Recovery time calculations indicate that the adsorption processes are comparatively stable, making these systems suitable for gas capture and pollution abatement. Overall, single-atom decoration provides an effective strategy to modulate the electronic structure and gas interactions of ZrS_2, highlighting its potential as an efficient gas scavenger for NO, NO_2, and SO_2.

Keywords: 1T-ZrS_2 monolayer; single-atom decoration; gas scavenger; COHP

check for updates

Academic Editor: Lyubov G. Bulusheva

Received: 26 September 2025
Revised: 27 October 2025
Accepted: 28 October 2025
Published: 29 October 2025

Citation: Wang, X.; Zhang, J.; Zhang, J.; Liu, X.; Lin, Y.; Li, F.; Wang, G.; Xu, Y.; Wang, P. 1T-ZrS_2 Monolayer Decorated with Sc, Ti, and V Single Atoms: A Potential Gas Scavenger for NO_x and SO_2. *Nanomaterials* **2025**, *15*, 1653. https://doi.org/10.3390/nano15211653

Copyright: © 2025 by the authors. Licensee MDPI, Basel, Switzerland. This article is an open access article distributed under the terms and conditions of the Creative Commons Attribution (CC BY) license (https://creativecommons.org/licenses/by/4.0/).

1. Introduction

With the intensification of industrialization and energy consumption, the emission of harmful gases such as nitrogen oxides NO_x (NO, NO_2) and sulfur dioxide (SO_2) into the atmosphere has continued to increase. These gaseous pollutants originate primarily from industrial combustion processes, vehicle exhaust emissions, and agricultural activities, which not only cause acid rain and photochemical smog but also pose serious threats to human health [1–5]. Therefore, developing efficient and stable gas sensing and capture materials is crucial for environmental remediation and the protection of human health [6–9].

Among various candidate materials, two-dimensional (2D) materials have attracted extensive attention owing to their high specific surface area, tunable electronic structures, and abundant active sites [10–14]. In particular, transition metal dichalcogenides (TMDCs), featuring layered crystal structures, adjustable band gaps, and excellent chemical

stability, are considered ideal materials for the adsorption and immobilization of toxic gases [15–22]. In recent years, numerous studies have focused on gas capture applications based on monolayer TMDCs. For example, Cho et al. systematically investigated the adsorption behaviors of toxic gases such as O_3, SO_2, and SO_3 on MoS_2 monolayers through combined experimental and theoretical approaches, demonstrating the great potential of MoS_2 for gas capture [23]. Similarly, Scardamaglia et al. experimentally synthesized WS_2 monolayers and demonstrated their high-sensitivity detection capability toward NO_2 molecules [24]. As a representative layered TMDC, ZrS_2 has been successfully fabricated in various nanostructured forms, exhibiting good structural stability and semiconducting characteristics [25–27]. Benefiting from its excellent optical, thermal, and electronic properties, ZrS_2 has been widely regarded as a promising candidate material for multifunctional applications [28–30]. For instance, Li et al. incorporated ZrS_2 into erbium-doped fiber lasers, achieving high-performance dual-wavelength Q-switched pulse outputs [31].

Extensive first-principles studies have demonstrated that single-atom modification can significantly tune the surface reactivity and electronic properties of TMDCs [32–38]. For example, Zhang et al. systematically investigated Co-, Pd-, and Pt-decorated MoS_2 monolayers and found that, compared with pristine MoS_2, these systems exhibit remarkably enhanced adsorption capabilities toward small molecules such as NO_2 and NH_3 [39]. This enhancement mainly arises from the strong hybridization between the metal *d* orbitals and the molecular orbitals of the adsorbates. Likewise, Ni-decorated WSe_2 monolayers exhibit significant modulation of electronic structures during CO and HCHO adsorption, indicating their potential as resistive-type gas sensing materials [40]. Pt- and Au-modified $ZrSe_2$ systems have also shown improved chemical adsorption and gas-sensing performances [41]. Furthermore, several studies have extended the single-atom decoration strategy to ZrS_2, revealing that transition metal decoration can significantly improve its gas adsorption and sensing behavior [42–44]. Notably, recent experimental advances have enabled the synthesis of several single-atom-modified TMDCs [45,46], which demonstrates the feasibility of preparing single-atom-decorated ZrS_2.

Motivated by this, we employ first-principles calculations to systematically investigate the adsorption behavior of NO, NO_2, and SO_2 molecules on Sc-, Ti-, and V-decorated 1T-ZrS_2 monolayers (1T denotes the trigonal phase of TMDCs with octahedral coordination). Sc, Ti, and V were selected as decorating atoms because they are located close to Zr in the periodic table and possess covalent radii slightly smaller than that of Zr, which may facilitate the experimental doping or surface decoration of ZrS_2. Moreover, recent experimental studies have demonstrated that Sc-, Ti-, and V-doped MoS_2 exhibit exceptional performance in photocatalytic nitrogen reduction [47], giant photoluminescence [48], and electrocatalytic hydrogen generation [49], respectively, motivating the hypothesis that these elements may also enhance gas adsorption upon decorating ZrS_2. We comprehensively analyze the influence of different adatom species on adsorption strength, charge transfer, geometric configuration, and potential dissociative adsorption behavior. In addition, binding energies, adsorption energies, density of states (DOS), crystal orbital Hamilton population (COHP), and electron localization function (ELF) analyses are performed to elucidate the underlying interaction mechanisms. Our results reveal that decoration with Sc, Ti, and V significantly enhances the chemisorption of NO, NO_2, and SO_2 on ZrS_2, demonstrating excellent gas capture performance and highlighting single-atom–decorated 1T-ZrS_2 as a promising gas scavenger for environmental remediation.

2. Computational Details

All density functional theory (DFT) calculations were performed using the Vienna ab initio Simulation Package (VASP5.4.4) [50–53]. The generalized gradient approximation

(GGA) with the Perdew–Burke–Ernzerhof (PBE) functional was employed to describe the exchange-correlation energy [54,55]. Spin polarization was included in all calculations. The DFT-D3 method was applied to account for van der Waals interactions between the ZrS_2 monolayer and the adsorbed gas molecules in the transition-metal-decorated systems [56]. The plane-wave cutoff energy was set to 600 eV. In the subsequent calculations, a $4 \times 4 \times 1$ ZrS_2 supercell containing 16 Zr atoms and 32 S atoms was adopted, as shown in Figure 1a. The Brillouin zone was sampled using a $3 \times 3 \times 1$ Γ-centered k-point mesh [57], while a denser $6 \times 6 \times 1$ k-point mesh was employed for the density of states (DOS) calculations to improve accuracy. The band structure and density of states of pristine ZrS_2 were calculated, showing a band gap of 1.21 eV with the GGA functional and 1.8 eV with the HSE06 hybrid functional, consistent with literature reports [58,59]. To avoid spurious interactions between periodic images, a vacuum spacing of 20 Å was introduced. Geometry optimization was considered converged when the maximum Hellmann-Feynman force on any atom fell below 0.01 eV/Å. During self-consistent-field (SCF) and electronic-property calculations, the energy convergence threshold was set to 1×10^{-6} eV.

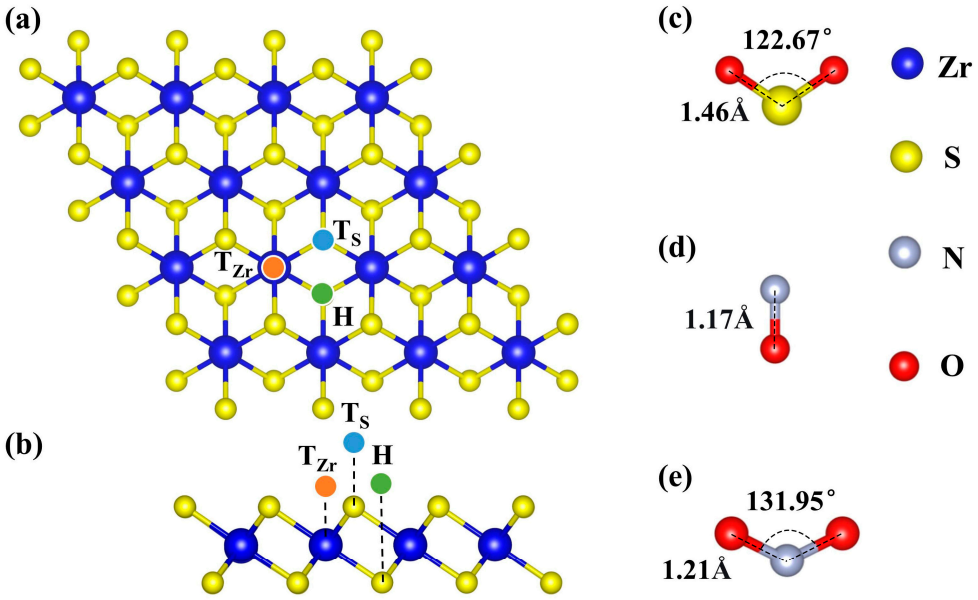

Figure 1. Optimized structures. (**a**,**b**) top and side views of initial ZrS_2 monolayer, respectively, and (**c**–**e**) Gas molecules SO_2, NO, and NO_2, respectively.

To identify the most stable adsorption configuration, the binding energy (E_{bind}) of a transition metal (TM) adatom on the ZrS_2 surface was calculated using the following equation:

$$E_{bind} = E_{TM\text{-}ZrS_2} - E_{TM} - E_{ZrS_2} \quad (1)$$

where E_{TM-ZrS_2}, E_{TM} and E_{ZrS_2} are the total energy of TM-ZrS_2 monolayer, TM atoms, and intrinsic ZrS_2 monolayer, respectively. In addition, E_{ads} was estimated to describe the adsorption between gas molecules and substrate, and the formula is as follows:

$$E_{ads} = E_{gas\text{-}substrate} - E_{gas} - E_{substrate} \quad (2)$$

where $E_{gas\text{-}substrate}$, E_{gas}, and $E_{substrate}$ represent the total energy of the adsorbed system, the energy of the gas molecules, and the energy of the substrate, respectively. A negative E_{ads} represents an energetically favorable adsorption process, whereas a positive E_{ads} corresponds to an energetically unfavorable one. A larger absolute value of the binding

energy (E_{bind}) or adsorption energy (E_{ads}) indicates stronger binding or adsorption and, consequently, a more stable system.

All subsequent computational post-processing was performed using VASPKIT [60], and the results were visualized with VESTA [61]. To further analyze bonding characteristics, the LOBSTER program [62] was employed to carry out the crystal orbital Hamilton population (COHP) methodology [63]. The Bader charge decomposition was carried out using the efficient algorithm developed by Henkelman and co-workers, in which the core charges were incorporated into the partitions [64–67]. In this analysis, the electron density was interpolated onto a refined grid of 240 × 240 × 320, and the number of electrons in the vacuum region was confirmed to be zero. To characterize the degree of electron localization and bonding nature, the electron localization function (ELF) [68,69] was employed, and its topological analysis was carried out using the CP2K2022.2 [70] package in conjunction with the Multiwfn3.8 program [71,72]. Additionally, to ensure that the projected density of states (PDOS) analysis was consistent with the crystal-field splitting reported in the previous studies [73,74], the qvasp script [75] was used to rotate the Cartesian coordinates so that each axis aligned along the Zr-S bond direction and corresponded with the octahedral framework surrounding the Zr atoms, thereby ensuring the accuracy of the subsequent electronic-structure analysis.

3. Results and Discussion

3.1. Geometry and Electronic Structure of the 1T-ZrS_2 Monolayer Decorated with Sc, Ti, and V Single Atoms

As shown in Figure 1, we optimized the structures of the pristine ZrS_2 monolayer and of the NO, NO_2, and SO_2 molecules. The optimized results indicate that the N-O bond length in the NO molecule is 1.16 Å, while both NO_2 and SO_2 adopt a bent (V-shaped) geometry, with N-O and S-O bond lengths of 1.22 Å and 1.48 Å, and O-N-O and O-S-O bond angles of 134.56° and 117.24°, respectively, consistent with previous reports [40,76,77]. The optimized lattice parameters of the ZrS_2 monolayer are $a = b = 3.69$ Å, with a Zr-S bond length of 2.58 Å, in good agreement with prior studies [78,79]. Three representative sites were considered as candidate decoration sites: atop Zr (T_{Zr}), atop S (T_S), and the hollow site (H), as shown in Figure 1a,b. Previous studies (Table 1) have shown that the adsorption of these three gases on pristine ZrS_2 is relatively weak [44,77,80], which is unfavorable for gas sensing or capture. Accordingly, we next systematically investigated ZrS_2 decorated with single TM atoms to enhance adsorption strength.

Table 1. Adsorption energies (E_{ads}) and charge transfer (Q_t) of three characteristic gases on ZrS_2 monolayer.

System	Gas Molecule	E_{ads} (eV)	Q_t (e)	Ref.
ZrS_2	NO	−0.298	-	[44]
ZrS_2	NO_2	−0.16	0.04	[77]
ZrS_2	SO_2	−0.52	0.01	[77]

Accordingly, we assessed Sc-, Ti-, and V-decoration of 1T-ZrS_2 across three candidate adsorption sites (Figure 1) and examined their effects on atomic geometry and electronic properties. The results show that when a TM atom is placed at the sulfur top site (T_S site), it relaxes to a nearby hollow site (H site), indicating that this configuration is energetically unstable. Therefore, subsequent analyses focused on the Zr top site (T_{Zr} site) and the hollow site (H site). As summarized in Table 2, all three transition metals prefer the hollow site, where the adsorption energy is the lowest (most negative), corroborating that the H site is the most stable adsorption site on the ZrS_2 monolayer. This conclusion is consistent with previous theoretical studies [73,74].

Table 2. Adsorption positions (T_{Zr}: TM adsorbed above a Zr atom, hollow: TM atom adsorbed above the lower-layer S atom), distance between the TM atom (TM = Sc, Ti, V) and its nearest S atom (d), binding energies (E_{bind}), Bader charge transfer (Q_t), and magnetic moments (M_{tot}) of TM-decorated ZrS_2.

System	Adsorption Position	d (Å)	E_{bind} (eV)	Q_t (e)	M_{tot}(μ_B)
Sc-ZrS_2	T_{Zr}	2.42	−4.82	1.25	0.39
	hollow	2.38	−5.16	1.10	0
Ti-ZrS_2	T_{Zr}	2.31	−4.90	0.94	0
	hollow	2.29	−5.35	0.81	0
V-ZrS_2	T_{Zr}	2.30	−3.71	0.81	2.18
	hollow	2.25	−4.16	0.58	0.94

The dynamical stability of all TM-decorated ZrS_2 systems was evaluated by calculating their phonon dispersion relations. As shown in Figure S1, using the Sc-decorated ZrS_2 system as a representative case, no imaginary frequencies were observed across the Brillouin zone, indicating that the hollow-site configuration is dynamically stable. These results further support selecting the hollow site as the most stable configuration for subsequent structural and electronic analyses.

Figure 2 shows the optimized structures of TM-decorated ZrS_2 monolayers at the hollow (H) sites, corresponding to the most stable adsorption sites discussed above. Upon TM decoration, only minor distortions of the hexagonal lattice are observed, and each TM atom forms stable TM-S bonds with neighboring S atoms. The bond lengths between the TM dopant atoms (Sc, Ti, and V) and their nearest neighboring S atoms are 2.38 Å, 2.29 Å, and 2.25 Å, respectively. Additionally, the Zr-S bonds adjacent to the dopants are noticeably elongated relative to the pristine value of 2.57 Å, reaching 2.70 Å, 2.79 Å, and 2.65 Å, respectively. Notably, in the Ti-decorated system, the Ti atom slightly embeds into the substrate lattice, causing the underlying S atom to move upward toward Ti. This is consistent with the most negative binding energy among the three, indicating a strong chemical adsorption between the Ti atom and the substrate. Bader analysis shows a net electron transfer from the adatom to ZrS_2: Sc, Ti, and V donate 1.10 e, 0.81 e, and 0.58 e, respectively. To visualize the charge redistribution, charge density difference (CDD) maps are plotted (Figure 2c,f,i).

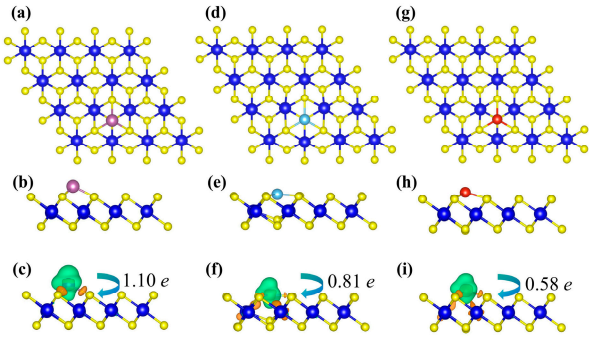

Figure 2. Panels (**a**,**d**,**g**) and (**b**,**e**,**h**) show the top and side views of the Sc-, Ti-, and V-decorated ZrS_2 systems, respectively. Panels (**c**,**f**,**i**) present the corresponding charge density difference diagrams. In these diagrams, orange and green isosurfaces denote charge accumulation and charge depletion, respectively, with corresponding isovalues of 0.007 e/Å^3, 0.009 e/Å^3, and 0.008 e/Å^3 for the Sc-, Ti-, and V-ZrS_2 systems.

To gain a deeper understanding of TM-modified ZrS_2, we further analyze the PDOS. In the 1T phase, each Zr atom is coordinated by six S atoms, forming an octahedral

coordination environment. Under this crystal field, the Zr *d* orbitals split into e_g and t_{2g} manifolds. When a TM atom is adsorbed on the ZrS_2 surface, it binds to the three nearest-neighbor S atoms. Although the other three coordination positions remain vacant, the TM atom still experiences an approximately octahedral crystal field close to O_h symmetry and thus exhibits similar orbital splitting [78,79]. To test this hypothesis, we rotated the Cartesian axes to the local octahedral orientation (x, y and z aligned with the Zr-S bonds) and calculated the PDOS to substantiate this interpretation.

As shown in Figure 3, the PDOS of the TM-decorated systems shows the characteristic octahedral crystal field splitting: d_{xy}, d_{yz} and d_{xz} form a t_{2g}-like set, whereas d_{z^2} and $d_{x^2-y^2}$ constitute an e_g-like set, as expected. Closer examination of the PDOS for the Sc-decorated system reveals hybridization at −3.85 eV and −4.96 eV. This system exhibits no significant spin splitting, and its total magnetic moment is 0 μ_B. In the Ti-decorated system, Ti *d* orbitals and S *p* orbitals exhibited hybridization at −2.47 eV and −4.56 eV, and pronounced hybridization was also present near the Fermi level (around −0.26 eV). The total magnetic moment is 0 μ_B. In contrast, the V-decorated system shows hybridization between V *d* orbitals and S *p* orbitals at −3.55 eV and −4.86 eV, along with pronounced hybridization near the Fermi level. Unlike the Sc- and Ti-decorated systems, the V-decorated system exhibited clear spin polarization, with a total magnetic moment of 0.94 μ_B, originating mainly from unpaired V 3*d* electrons. As seen in the figure, hybridization near the Fermi level in TM-decorated systems is dominated by t_{2g} orbitals, whereas e_g orbitals contribute less. Moreover, with increasing *d*-electron count of the TM atom, the occupancy of *d* orbitals near the Fermi level increased, and the hybridization strength of both t_{2g} and e_g orbitals was enhanced.

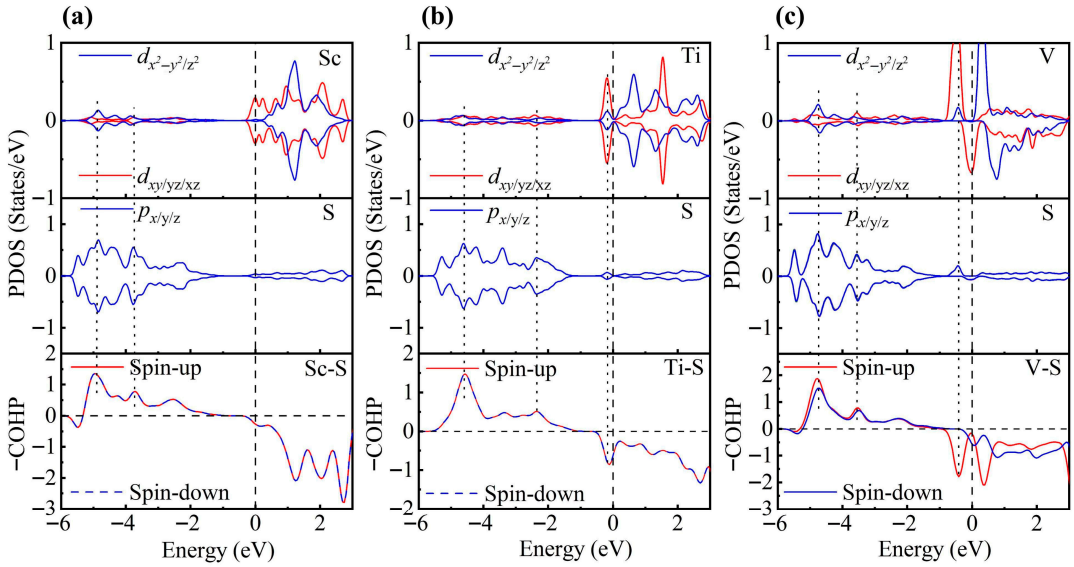

Figure 3. PDOS and COHP of (**a**) Sc-, (**b**) Ti-, and (**c**) V-decorated ZrS_2 monolayers. DOS showing orbital degeneracy between TM $d_{xy}/d_{yz}/d_{xz}$ and S $p_x/p_y/p_z$ orbitals, as well as additional degeneracy of d_{z^2} and $d_{x^2-y^2}$ orbitals below the Fermi level.

To gain deeper insight into the interaction between TM atoms and the substrate, we calculated the COHP between TM atoms and neighboring S atoms. In the COHP analysis, the Fermi level is set to 0 eV, with positive values representing bonding states and negative values representing antibonding states. The integrated COHP (ICOHP) below the Fermi level quantifies bond strength, so that more negative values (i.e., larger absolute values) indicate stronger bonding, thereby reflecting the relative strength of atomic interactions. As shown in Figure 3, the V-decorated system exhibits pronounced antibonding states near the Fermi level due to its larger number of *d* electrons, whereas the Sc- and Ti-decorated

systems are dominated by bonding states below the Fermi level, with fewer antibonding contributions. Consequently, the V-decorated system has the smallest ICOHP absolute value, corresponding to the weakest adsorption strength. Further analysis reveals that the Sc-decorated system not only shows antibonding states at the Fermi level but also features an additional antibonding peak around −5.46 eV; in contrast, the Ti-decorated system exhibits antibonding states only near the Fermi level. As a result, the Ti-decorated system presents the largest ICOHP absolute value, corresponding to the strongest adsorption and the most significant structural distortion. Specifically, the ICOHP values of the V-, Sc-, and Ti-decorated systems are −4.53 eV, −4.78 eV, and −4.98 eV, respectively, in excellent agreement with the corresponding adsorption energy trends.

3.2. Adsorption of NO on TM-Decorated 1T-ZrS_2 Monolayers

To gain deeper insight into the influence of TM decoration on the gas-adsorption capability, the adsorption behaviors of NO, NO_2, and SO_2 molecules on TM-decorated ZrS_2 monolayers were systematically investigated. As illustrated in Figure 4a–c, the NO molecule binds through the N atom to Sc-, Ti-, and V-decorated ZrS_2, with TM-N bond lengths of 2.01, 1.82, and 1.53 Å, respectively. After adsorption, the N-O bond length of NO is elongated relative to its optimized value of 1.17 Å, increasing to 1.20, 1.20, and 1.19 Å, respectively. This elongation indicates that the interaction with the TM weakens the intrinsic N–O bond.

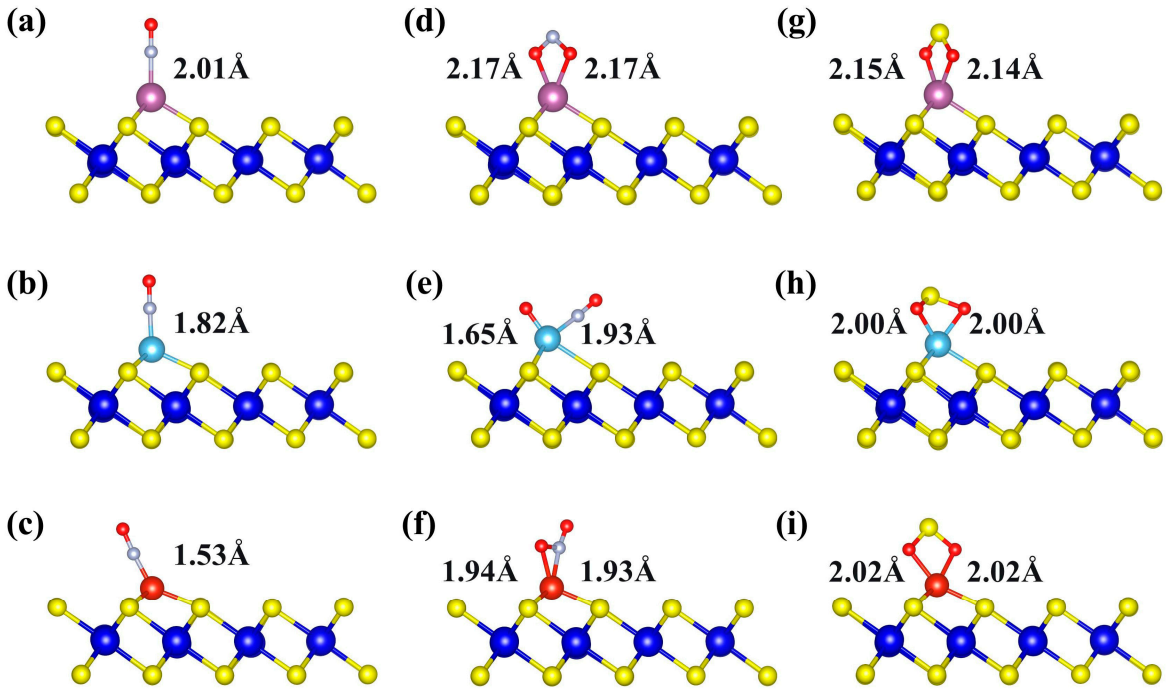

Figure 4. The most stable adsorption structures of three gases on Sc-, Ti-, and V-decorated ZrS_2 monolayers: (**a**–**c**) NO adsorption on Sc-, Ti-, and V-ZrS_2, respectively; (**d**–**f**) NO_2 adsorption on Sc-, Ti-, and V-ZrS_2, respectively; and (**g**–**i**) SO_2 adsorption on Sc-, Ti-, and V-ZrS_2, respectively.

To elucidate the adsorption mechanism, we analyzed the PDOS. As shown in Figure 5, for NO adsorbed on Sc-ZrS_2, a pronounced orbital hybridization appears at approximately −0.83 eV below the Fermi level, with contributions from both the t_{2g} and e_g orbitals. The COHP results indicate bonding interactions in this energy region, and the calculated adsorption energy is −2.10 eV. For the Ti-decorated system, in addition to the hybridization between the spin-up orbitals of Ti-*d* and N-*p* states at −0.5 eV, a spin-up bonding state is also present at the Fermi level. This enhances the adsorption, yielding an adsorption energy

of −2.47 eV. For the V-decorated system, bonding states appear in both spin up and down channels at approximately −0.76 eV, which further strengthens the adsorption and results in an adsorption energy of −2.89 eV. Moreover, the adsorption strength tends to increase with increasing *d*-electron count, which is likely due to enhanced interaction between the N *p* orbitals and the TM *d* orbitals. Compared with the adsorption energy on the pristine ZrS_2 monolayer (–0.298 eV) [44], the adsorption energies on TM-decorated ZrS_2 are significantly enhanced, indicating that TM decoration plays a crucial role in improving the adsorption capability of ZrS_2.

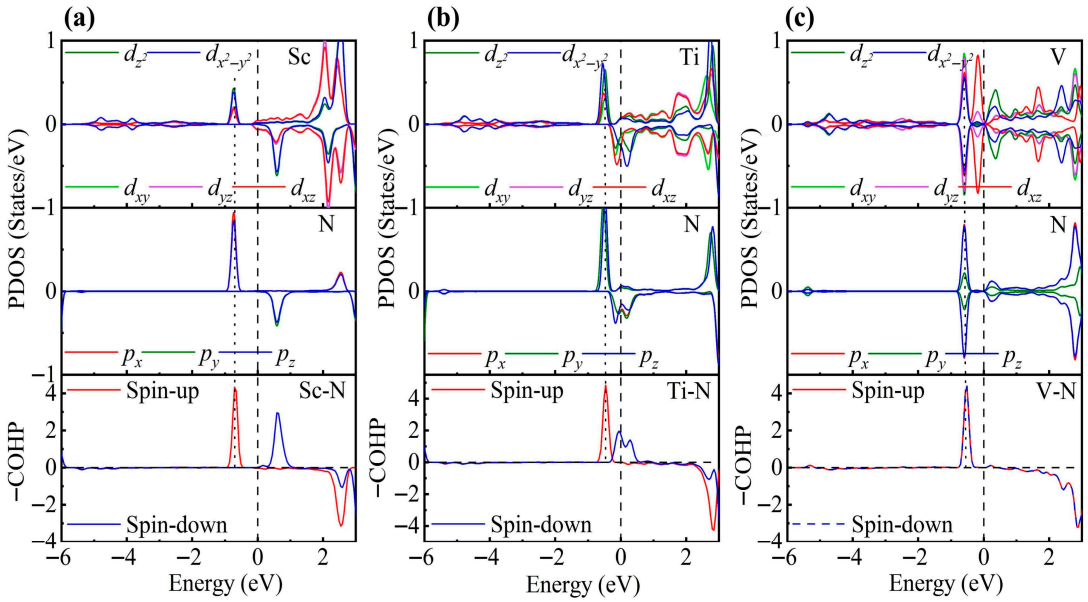

Figure 5. PDOS and COHP for NO adsorption on (**a**) Sc-, (**b**) Ti-, and (**c**) V-decorated ZrS_2 monolayers. The DOS reveals partial degeneracy of the TM $d_{xy}/d_{yz}/d_{xz}$ orbitals and the N $p_x/p_y/p_z$ orbitals.

As shown in Figure S2, the CDD indicates electron depletion around the transition metal atoms and accumulation on the NO molecule. Further Bader charge analysis reveals charge transfers of 0.47 e, 0.51 e, and 0.48 e to the NO molecule in the Sc-, Ti-, and V-decorated systems, respectively. To elucidate the bonding between NO and the TM atom, we further performed ELF calculations (Figure 6). ELF ranges from 0 to 1: values near 1 denote highly localized electron pairs (covalent bonds or lone pairs); values around 0.5 indicate uniform electron gas; and values near 0 denote very weak localization or very low electron density. As shown, the ELF values are relatively high around the NO molecule, indicating strong electron localization, whereas the regions near the decorated metal atoms exhibit slightly weaker electron localization. Furthermore, the ELF topological analysis (Figure S3a–c) identifies multiple (3, −3) critical points (CPs; ELF attractors) in the N-TM interaction region that lie off the N-TM internuclear line. Moreover, considering the torus-shaped ELF around N (Figure S3d–f), together with the previously discussed PDOS/COHP signatures of orbital hybridization, the NO-TM interaction is likely governed primarily by π-type character.

Furthermore, changes in the magnetic properties were observed upon NO adsorption. For the Sc- and Ti-decorated systems, NO adsorption induces net magnetic moments of 1.96 μ_B and 0.59 μ_B, respectively. The reduced net moment in the Ti-decorated system relative to Sc is attributed to partial occupation of spin-down states in the occupied region. For the V-decorated system, NO adsorption reduces the magnetic moment from 0.94 μ_B to a negligible value, rendering the system effectively nonmagnetic.

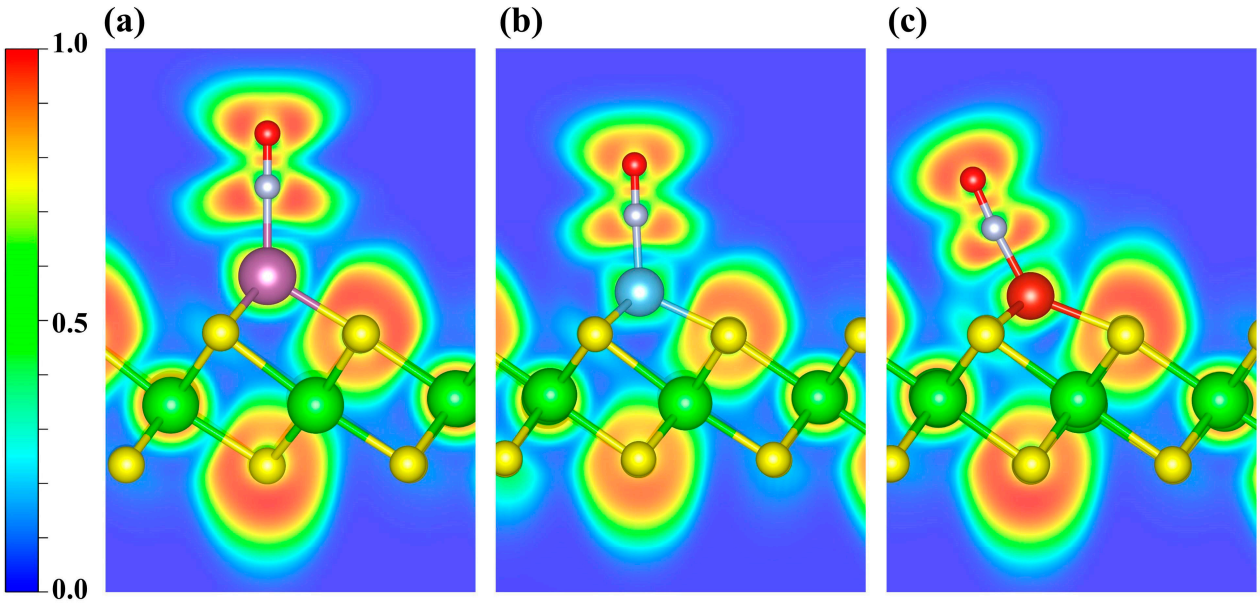

Figure 6. ELF distributions of NO adsorbed on (**a**) Sc-, (**b**) Ti-, and (**c**) V-decorated ZrS_2 systems. The plots highlight the ELF features around the adsorption sites. Blue and red denote ELF values of 0 and 1, respectively.

3.3. Adsorption of NO_2 on TM-Decorated 1T-ZrS_2 Monolayers

To elucidate the interaction of NO_2 with Sc-, Ti-, and V-decorated ZrS_2 monolayers, we first analyzed the optimized adsorption geometries (Figure 4d–f). The results show that NO_2 is molecularly adsorbed on Sc-ZrS_2 and V-ZrS_2, whereas a dissociative adsorption final state is stabilized on Ti-ZrS_2. In the molecular state, NO_2 binds in a bidentate fashion: O, O-chelation on Sc and O, N-chelation on V. In contrast, on Ti the adsorbate splits into O and NO fragments: one O forms a Ti-O bond, the N atom of the NO fragment forms a Ti-N bond, and the remaining O stays bonded to N within the NO fragment. Representative bond lengths are Sc-O ≈ 2.17 Å (two bonds), Ti-N = 1.93 Å, Ti-O = 1.65 Å, V-N = 1.92 Å, and V-O = 1.94 Å, consistent with the above configurations.

As summarized in Table 3, NO_2 binds most strongly on the Ti-decorated system, with an adsorption energy of −3.63 eV, substantially larger in magnitude than on Sc (−3.08 eV) and V (−2.70 eV). As shown in Figure S4, the CDD indicates that during NO_2 adsorption, electron depletion occurs around the TM atoms, while electron accumulation develops on the molecule, facilitating bond formation between NO_2 and the TM atom. Further Bader charge analysis reveals that Sc and V transfer 0.67 e and 0.56 e to NO_2, respectively, whereas Ti exhibits the largest charge transfer of 1.08 e, nearly twice that of V. This pronounced electron redistribution weakens the intramolecular N-O bonds, providing favorable thermodynamic conditions for NO_2 dissociation. Moreover, the adsorption energies of NO_2 on all three TM-decorated systems are significantly higher than that on the pristine ZrS_2 monolayer (−0.16 eV), and the corresponding charge transfers are also markedly larger than that for NO_2 adsorption on pristine ZrS_2 (0.04 e) [77], further demonstrating that TM decoration can substantially enhance the adsorption capability of ZrS_2.

Table 3. Adsorption energy (E_{ads}), charge transfer (Q_2), adsorption distance (D), gas molecular bond length (d), total magnetic moment (M_{tot}), and ICOHP for the adsorption of three representative gases (NO, NO_2, and SO_2) on Sc-, Ti-, and V-decorated ZrS_2 monolayers.

Gas Molecule	Atom	E_{ads} (eV)	Q_t (e)	D (Å)	d (Å)	M_{tot} (μ_B)	ICOHP (eV)
NO	Sc	−2.10	0.47	2.01	1.20	1.96	−2.17
	Ti	−2.47	0.51	1.82	1.20	0.59	−3.16
	V	−2.89	0.48	1.53	1.19	0	−3.30
NO_2	Sc	−3.08	0.67	2.17	1.29	0	−2.32
	Ti	−3.63	1.08	1.65/1.93	1.17	0.04	−7.00
	V	−2.70	0.56	1.93/1.94	1.38/1.20	1.99	−2.94
SO_2	Sc	−2.28	0.71	2.14/2.15	1.55	0.97	−2.54
	Ti	−2.21	0.73	2.00	1.61	0	−3.24
	V	−1.63	0.63	2.02	1.56	2.96	−2.61

Electronic structure analysis clearly reveals that TM decoration significantly enhances the gas adsorption capability of ZrS_2. As shown in Figure 7, in the Ti-decorated system, the Ti 3*d* states strongly hybridize with the N-*p* and O-*p* orbitals near the Fermi level: the Ti e_g states hybridize with N-p_y at −0.36 eV, and the Ti d_{z^2} state couples with O-*p* at −2.74 eV, forming stable bonding states. Such strong *d*–*p* interactions promote electron transfer from the Ti atom to NO_2, effectively populating the N-O antibonding orbital, thereby weakening the N-O bond and driving its dissociation. In contrast, the Sc-decorated system exhibits weak *d*-*p* hybridization only at deeper energy levels (−2.05, −3.18, and −3.90 eV), with nearly no contribution near the Fermi level, whereas the V-decorated system shows limited hybridization with O-$p_{y/z}$ orbitals around −3.87 eV and only weak interaction near the Fermi level. Consequently, NO_2 remains in a molecular adsorption state on Sc- and V-decorated surfaces but undergoes dissociative adsorption on the Ti-decorated surface.

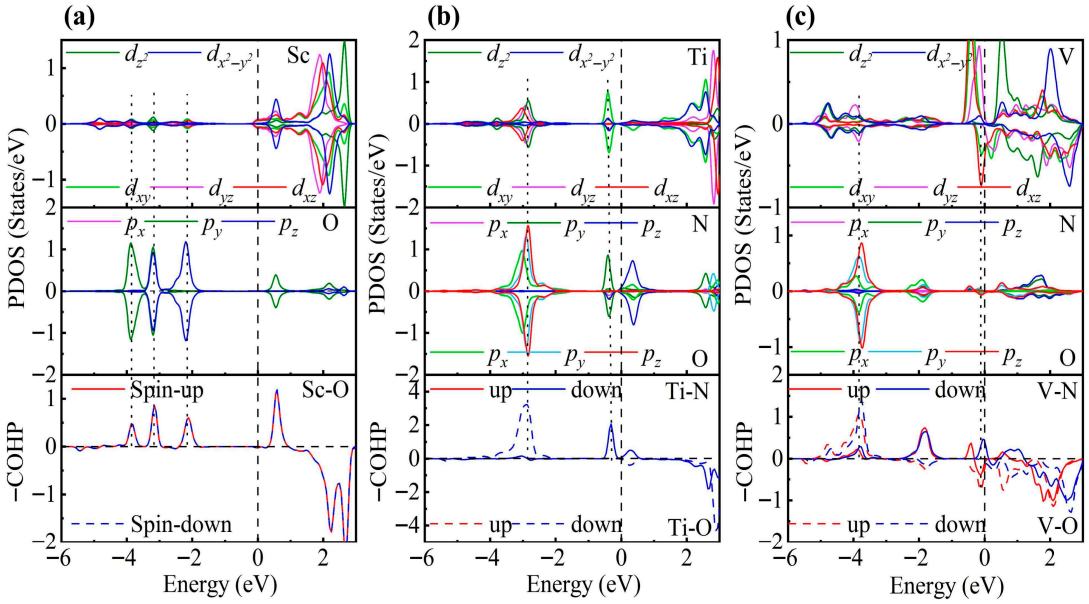

Figure 7. PDOS and COHP for NO_2 adsorption on (**a**) Sc-, (**b**) Ti-, and (**c**) V-decorated ZrS_2 monolayers. The DOS reveals partial degeneracy between the TM $d_{xy}/d_{yz}/d_{xz}$ orbitals and the $p_x/p_y/p_z$ orbitals of N and O.

COHP analysis further substantiates this trend. All three TM-decorated systems enhance the orbital hybridization between NO_2 and the substrate, but the effect is strongest for Ti. Both Ti-O and Ti-N bonds show pronounced bonding contributions near the Fermi

level, with more negative −ICOHP values and larger integrated bonding areas, which together stabilize the dissociative adsorption state. By contrast, Sc exhibits relatively weak bonding peaks, and V even displays antibonding features at the Fermi level, which weakens the metal-ligand interactions. Mechanistically, the cooperative Ti-O/Ti-N bonding channels facilitate electron transfer from the intrinsic N-O bonding orbital to the newly formed metal-ligand bonds, thereby weakening the internal N-O interaction and promoting cleavage. For Sc and V, insufficient *d*-*p* overlap or higher *d*-orbital occupation prevents the formation of such strong multicenter bonding.

In Figure 8, the ELF maps display pronounced localization around the N and O atoms of NO_2. To further investigate the bonding interactions, an ELF topological analysis was carried out (Figure S5a–c). It is revealed that the (3, −3) CPs between Sc and the two O atoms lie along their respective internuclear axes (Figure S5a), indicating that both Sc-O bonds are consistent with σ-dominated covalent bonds. However, similar to the case of NO, in the Ti- and V-decorated systems the (3, −3) CPs for TM-O and TM-N lie off the internuclear axis (Figure S5b,c). Taken together with the previously discussed PDOS/COHP evidence for orbital hybridization, the interactions are likely governed primarily by π-type character.

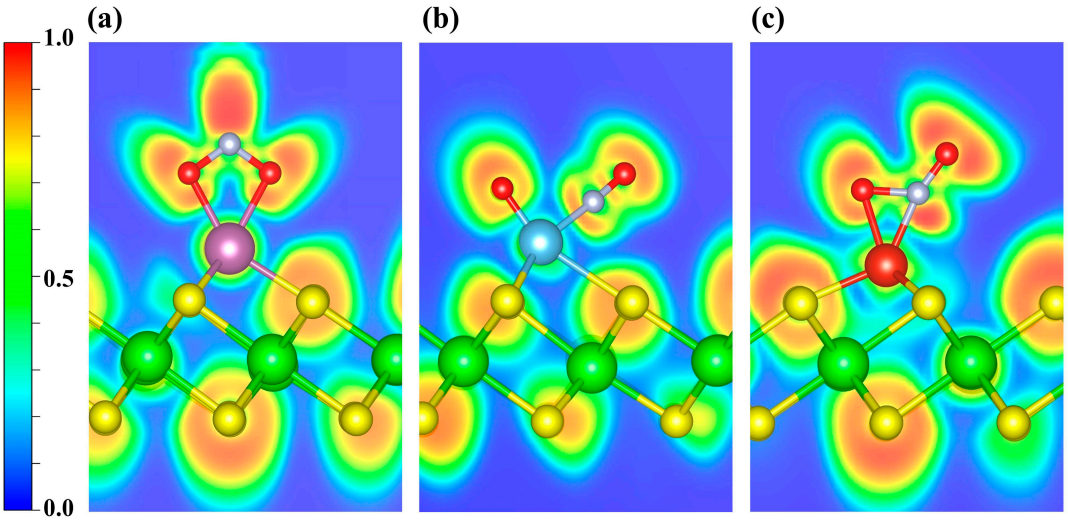

Figure 8. ELF distributions of NO_2 adsorbed on (**a**) Sc-, (**b**) Ti-, and (**c**) V-decorated ZrS_2 systems. The plots highlight the ELF features around the adsorption sites. Blue and red denote ELF values of 0 and 1, respectively.

3.4. Adsorption of SO_2 on TM-Decorated 1T-ZrS_2 Monolayers

As shown in Figure 4g–i, SO_2 molecules are stably adsorbed on Sc-, Ti- and V-decorated ZrS_2 monolayers via bonds formed between the two oxygen atoms and the TM atoms. The bond lengths are 2.15 Å and 2.14 Å for Sc-O, 2.00 Å for Ti-O, and 2.02 Å for V-O, indicating a gradual shortening as the atomic number of the TM atom increases. Conventionally, shorter bond lengths are expected to correspond to stronger adsorption. However, the adsorption energies show the opposite trend, with the absolute values decreasing in sequence: Sc, −2.28 eV; Ti, −2.21 eV; V, −1.63 eV. This finding indicates that bond-length reduction alone does not determine adsorption strength, and the adsorption behavior is primarily governed by the electronic structure and orbital interactions of the system.

The CDD and Bader charge analysis further indicate that transition metal modification significantly enhances the adsorption of SO_2 on the ZrS_2 surface (Figure S6). During adsorption, the CDD shows electron depletion around the transition metal atoms, while electron accumulation occurs on the SO_2 molecule, resulting in a stable chemical interaction between the molecule and the TM atom. Bader charge analysis reveals that 0.71 e and 0.73 e are transferred to SO_2 in the Sc- and Ti-decorated systems, respectively, while

the charge transfer is slightly lower in the V-decorated system, at 0.63 e. Consistently, the ICOHP calculations show that the Ti-O interaction is the strongest (−3.24 eV), while the interactions in the Sc and V systems are relatively weaker (−2.54 eV and −2.61 eV, respectively), as listed in Table 3. In contrast, the adsorption energy of SO_2 on pristine ZrS_2 is only −0.52 eV, with a charge transfer of merely 0.01 e [77], significantly lower than those of the TM-modified systems.

The PDOS and COHP analyses further support this conclusion (Figure 9). In the Sc-modified system, a pronounced hybridization between Sc *d* and O p_y orbitals is observed at −0.86 eV, corresponding to a spin-up bonding state, while at −3.90 eV, Sc *d* and O *p* orbitals also exhibit significant hybridization, forming both spin-up and spin-down bonding states. The absence of notable antibonding states near the Fermi level ensures the stability of adsorption. In the Ti-modified system, Ti t_{2g} orbitals hybridize with O *p* orbitals at −1.05 eV, and stronger Ti *d*-O *p* hybridizations are observed at −3.08 eV, −3.91 eV, and −4.45 eV, with the largest COHP area at −4.45 eV. Despite the presence of weak antibonding states near the Fermi level, the bonding states dominate, resulting in strong adsorption. In contrast, the V-modified system exhibits pronounced occupation of antibonding states near the Fermi level, mainly involving t_{2g} orbitals, with the strongest V *d*-O *p* hybridization at −3.82 eV. The increased d-electron count reduces the covalent contribution, explaining the significantly lower adsorption energy compared to the Sc- and Ti-modified systems.

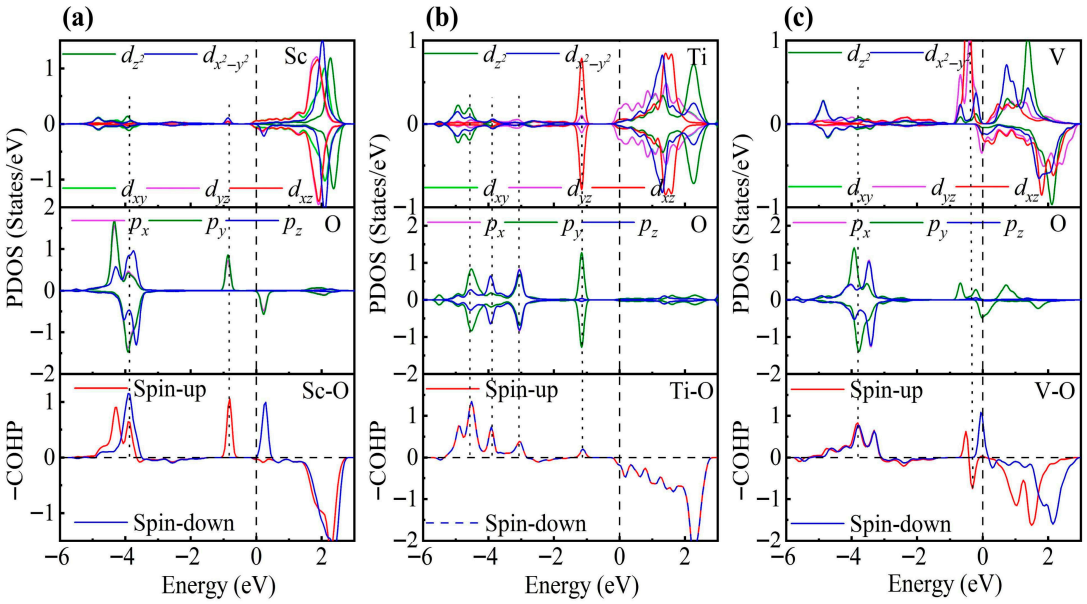

Figure 9. PDOS and COHP for SO_2 adsorption on (**a**) Sc-, (**b**) Ti-, and (**c**) V-decorated ZrS_2 monolayers. The DOS reveals partial degeneracy of the TM $d_{xy}/d_{yz}/d_{xz}$ orbitals and the O $p_x/p_y/p_z$ orbitals.

Figure 10 shows the ELF maps for SO_2 adsorbed on Sc-, Ti-, and V-decorated surfaces, in which the regions around the S and O atoms exhibit pronounced electron localization. An ELF topological analysis (Figure S7a–c) shows that, in the Sc- and V-decorated systems, the (3, −3) CPs lie along the TM-O bond direction (Figure S7a,c), which is consistent with a predominantly σ-type covalent character. In contrast, for SO_2 adsorption on the Ti-decorated ZrS_2, the (3, −3) CPs are located outside the bonding axis (Figure S7b). However, given the relatively strong electron localization in the region between Ti and O (Figures 10b and S7e), together with the PDOS/COHP analyses discussed above, we infer that a covalent component also contributes to the Ti-O interaction.

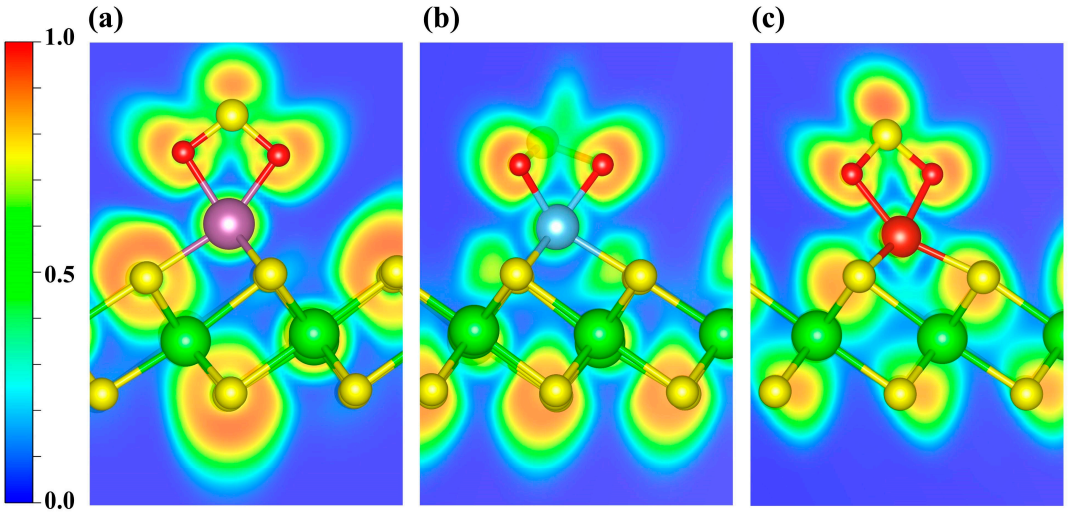

Figure 10. ELF distributions of SO_2 adsorbed on (**a**) Sc-, (**b**) Ti-, and (**c**) V-decorated ZrS_2 systems. The plots highlight the ELF features around the adsorption sites. Blue and red denote ELF values of 0 and 1, respectively.

Notably, SO_2 adsorption modifies the bonding characteristics and significantly affects the magnetic properties of the systems. For Sc-decorated ZrS_2, which is nonmagnetic prior to adsorption, a magnetic moment of 0.97 μ_B appears after SO_2 adsorption (Table 3). DOS analysis indicates that the observed moment primarily arises from the SO_2 molecule, as the O *s* and p_y orbitals near the Fermi level show preferential occupation by spin up electrons, inducing local spin polarization. In contrast, V decorated ZrS_2 has a magnetic moment of 0.94 μ_B before adsorption, which increases markedly to 2.96 μ_B after SO_2 adsorption. The DOS results indicate that this enhancement mainly arises from strong hybridization between V d_{xz} and d_{yz} orbitals and O p_y orbitals. This observation further confirms that the strong interaction between SO_2 and transition metal decorated ZrS_2 is crucial for tuning the magnetic properties of the system.

3.5. Gas Sensing Properties of TM-Decorated 1T-ZrS_2 Monolayers

The recovery time is an important parameter for gas sensors, which is directly related to the adsorption properties of the material and the sensor's reusability [81]. The recovery time affects the sensor response speed and also determines its stability and reliability in practical applications. As shown in Figure 11, ZrS_2 monolayers decorated with TM (Sc, Ti and V) show significantly different recovery times for NO, NO_2 and SO_2. The recovery time (τ) was estimated using the van't Hoff-Arrhenius relation within the framework of transition state theory, as expressed by [82]:

$$\tau = {\nu_0}^{-1} e^{(-E_{ads}/k_B T)} \quad (3)$$

where ν_0 is the attempt frequency (typically on the order of 1×10^{12} s^{-1} [83]), E_{ads} is the adsorption energy, k_B is the Boltzmann constant (8.617×10^{-5} $eV \cdot K^{-1}$), and T is the absolute temperature. Here, the recovery times are calculated at three different temperatures: 300 K, 400 K, and 500 K.

The computational results show that at room temperature (300 K) the shortest recovery time calculated for NO desorption from TM decorated ZrS_2 is 1.9×10^{23} s, which is a consequence of the high adsorption energy of NO on the substrate (see Table 3). This result indicates that TM decorated ZrS_2 can effectively capture NO, but NO is difficult to desorb from this substrate within a short time, which makes the material unsuitable for reversible gas sensing in typical sensor applications. Raising the operating temperature reduces the

recovery time; however, even at 400 K and 500 K the desorption remains slow compared with time scales relevant for practical sensing.

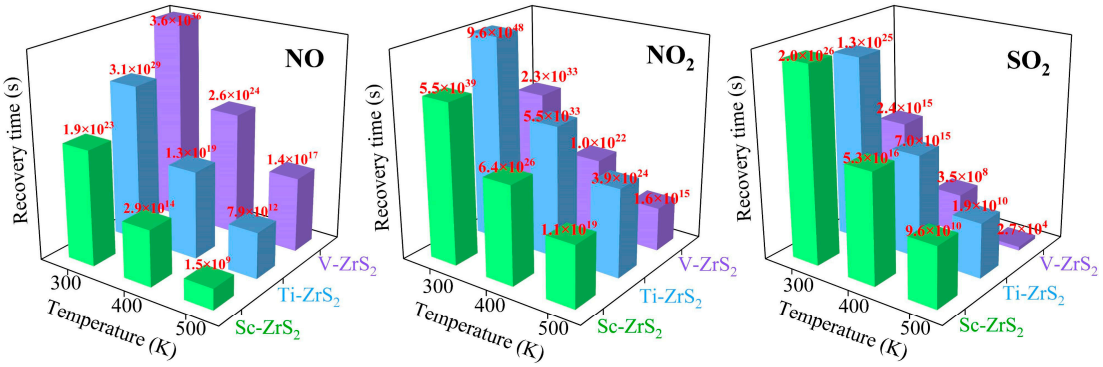

Figure 11. The calculated recovery time (τ) for the desorption of NO, NO_2, and SO_2 molecules from Sc-, Ti-, and V-decorated ZrS_2 monolayers at various temperatures (300 K to 500 K).

For NO_2 and SO_2, the shortest recovery times are observed in the V-decorated ZrS_2 system at 500 K, being 1.6×10^{15} s and 2.7×10^4 s, respectively; these values correspond approximately to 5.07×10^7 years for NO_2 and 7.5 h for SO_2. Such long recovery times, particularly the extremely long value for NO_2, indicate that V-decorated ZrS_2 is unsuitable for reversible gas sensing but may have potential for gas capture or storage applications.

It is worth noting that using the desorption barrier instead of the adsorption energy may yield a more rigorous estimation of recovery time. However, for the systems studied here, the desorption barrier obtained via CI-NEB and the adsorption energy differ by only about 0.1 eV. A similar difference has been reported for CO adsorption on Pt(111) [84]. Therefore, substituting the desorption barrier into the van't Hoff-Arrhenius relation does not alter the overall conclusions regarding the gas-capture capability of ZrS_2. Consequently, employing the adsorption energy as an approximation for the desorption barrier is a reasonable and widely adopted approach for estimating recovery behavior.

Compared with the adsorption of NO, NO_2, and SO_2 on pristine ZrS_2, the recovery times of these gases on the transition-metal-decorated structures are significantly prolonged (see Table S1), indicating that the gas desorption process becomes more difficult after decoration. Overall, TM-decorated ZrS_2 exhibits predominantly irreversible adsorption and slow desorption for all three gases, resulting in poor reusability and rendering the material unsuitable for reversible gas sensing under typical operating conditions. However, the long recovery times indicate strong adsorption, suggesting that TM-decorated ZrS_2 has potential for gas capture and environmental remediation. Notably, Ti-decorated ZrS_2 shows catalytic activity toward NO_2, where the adsorbed molecule undergoes surface dissociation, implying its potential for catalytic degradation or conversion of harmful gases. Therefore, beyond conventional sensing applications, TM-decorated ZrS_2 may find use in gas capture, storage, environmental cleanup, and catalytic processes. Future studies should focus on optimizing the adsorption–desorption kinetics to balance strong gas capture with controllable desorption, facilitating practical applications in industrial and environmental contexts.

4. Conclusions

In summary, we investigated the adsorption of NO, NO_2, and SO_2 on Sc-, Ti-, and V-decorated 1T-ZrS_2 by first-principles calculations. The decorating metals preferentially occupy the hexagonal hollow site of ZrS_2 and generate an approximately octahedral coordination environment, giving rise to characteristic *d*-orbital splitting. Transition-metal decoration markedly strengthens gas adsorption; notably, Ti decoration yields the strongest

interaction with NO_2 (E_{ads} = −3.63 eV) and drives dissociative adsorption, indicating catalytic activation of NO_2 on Ti-decorated ZrS_2. Electronic structure analyses indicate pronounced metal-to-adsorbate electron donation and robust hybridization between metal *d* and molecular *p* orbitals, which together underpin the stability of the adsorbed states. Within the investigated temperature range, Sc-, Ti-, and V-decorated ZrS_2 exhibit relatively long recovery times for NO, NO_2, and SO_2, indicating strong adsorption stability and high gas-capture capability. From a practical perspective, Sc, Ti, and V are earth-abundant and less toxic compared with certain heavy metals, making them promising candidates for environmentally sustainable modification of ZrS_2. Nevertheless, future work should assess their environmental stability before large-scale applications.

Supplementary Materials: The following supporting information can be downloaded at: https://www.mdpi.com/article/10.3390/nano15211653/s1, Figure S1. The calculated phonon dispersion of Sc-decorated 1T-ZrS_2, evidencing the dynamical stability of the structure. Figure S2. The top and side views of the charge density difference for NO adsorbed on (a) Sc-, (b) Ti-, and (c) V-decorated ZrS_2 systems. In these diagrams, orange and green isosurfaces denote charge accumulation and charge depletion, respectively, with an isovalue of 0.008 e/Å^3. Figure S3. Topological analyses of the ELF for NO adsorption on (a) Sc-, (b) Ti-, and (c) V-decorated ZrS_2. The purple dots represent (3, −3) critical points (CPs), corresponding to local maxima in the ELF. Only the CPs near the decorated atoms and the gas molecule are shown. The chemical bonds were generated by the analysis software, and some bonding representations may contain visualization errors. (d–f) depict the corresponding 3D isosurface representations of the ELF, where n denotes the isosurface value. Figure S4. The top and side views of the charge density difference for NO_2 adsorbed on (a) Sc-, (b) Ti-, and (c) V-decorated ZrS_2 systems. In these diagrams, orange and green isosurfaces denote charge accumulation and charge depletion, respectively, with an isovalue of 0.008 e/Å^3. Figure S5. Topological analyses of the ELF for NO_2 adsorption on (a) Sc-, (b) Ti-, and (c) V-decorated ZrS_2. The purple dots represent (3, −3) critical points (CPs), corresponding to local maxima in the ELF. Only the CPs near the decorated atoms and the gas molecule are shown. The chemical bonds were generated by the analysis software, and some bonding representations may contain visualization errors. (d–f) depict the corresponding 3D isosurface representations of the ELF, where n denotes the isosurface value. Figure S6. The top and side views of the charge density difference for SO_2 adsorbed on (a) Sc-, (b) Ti-, and (c) V-decorated ZrS_2 systems. In these diagrams, orange and green isosurfaces denote charge accumulation and charge depletion, respectively, with an isovalue of 0.008 e/Å^3. Figure S7. Topological analyses of the ELF for SO_2 adsorption on (a) Sc-, (b) Ti-, and (c) V-decorated ZrS_2. The purple dots represent (3, −3) critical points (CPs), corresponding to local maxima in the ELF. Only the CPs near the decorated atoms and the gas molecule are shown. The chemical bonds were generated by the analysis software, and some bonding representations may contain visualization errors. (d–f) depict the corresponding 3D isosurface representations of the ELF, where n denotes the isosurface value. Table S1. The recovery times (τ) of NO, NO_2, and SO_2 adsorbed on pristine ZrS_2, with *T* denoting the adsorption temperature (300, 400, 500 K).

Author Contributions: X.W. and J.Z. (Jiaqi Zhang) implemented the computational study, conducted DFT calculations and analyses, prepared the figures, and wrote the first draft. X.L., Y.L., F.L. and Y.X. contributed to formal analysis, validation, and visualization. P.W., J.Z. (Jinjuan Zhang) and G.W. conceived the idea and supervised the project. All authors have read and agreed to the published version of the manuscript.

Funding: This work is supported by the Natural Science Foundation of Shandong Province (Nos. ZR2021QA031, ZR2024QA213), the National Natural Science Foundation of China (No. 12504282), the Postdoctoral Fellowship Program of CPSF (No. GZC20240951), and Qingdao Postdoctoral Project Funding (No. QDBSH20240102115).

Data Availability Statement: The data is available on the request from corresponding author.

Conflicts of Interest: We declare that we have no known competing financial interests or personal relationships that could have appeared to influence the work reported in this paper.

References

1. Jion, M.M.F.; Jannat, J.N.; Mia, M.Y.; Ali, M.A.; Islam, M.S.; Ibrahim, S.M.; Pal, S.C.; Islam, A.; Sarker, A.; Malafaia, G.; et al. A Critical Review and Prospect of NO_2 and SO_2 Pollution over Asia: Hotspots, Trends, and Sources. *Sci. Total Environ.* **2023**, *876*, 162851. [CrossRef]
2. Lewis, A.; Edwards, P. Validate Personal Air-Pollution Sensors. *Nature* **2016**, *535*, 29–31. [CrossRef]
3. Yang, J.; Sun, R.; Bao, X.; Liu, J.; Ng, J.W.; Tang, B.; Liu, Z. Enhancing Selectivity of Two-Dimensional Materials-Based Gas Sensors. *Adv. Funct. Mater.* **2025**, *35*, 2420393. [CrossRef]
4. Feng, Q.; Huang, B.; Li, X. Graphene-Based Heterostructure Composite Sensing Materials for Detection of Nitrogen-Containing Harmful Gases. *Adv. Funct. Mater.* **2021**, *31*, 2104058. [CrossRef]
5. Tyagi, D.; Wang, H.; Huang, W.; Hu, L.; Tang, Y.; Guo, Z.; Ouyang, Z.; Zhang, H. Recent Advances in Two-Dimensional-Material-Based Sensing Technology toward Health and Environmental Monitoring Applications. *Nanoscale* **2020**, *12*, 3535–3559. [CrossRef] [PubMed]
6. Cui, H.; Zhang, G.; Zhang, X.; Tang, J. Rh-Doped $MoSe_2$ as a Toxic Gas Scavenger: A First-Principles Study. *Nanoscale Adv.* **2019**, *1*, 772–780. [CrossRef] [PubMed]
7. Luo, L.; Guo, Y.; Zhu, T.; Zheng, Y. Adsorption Species Distribution and Multicomponent Adsorption Mechanism of SO_2, NO, and CO_2 on Commercial Adsorbents. *Energy Fuels* **2017**, *31*, 11026–11033. [CrossRef]
8. Zheng, R.; Qiu, L.; Zhou, X.; Liu, X.; Wang, Q.; Wang, C.; Zhu, T.; Chang, H. Research Progress in CO_2 and NO_x Adsorption by Two-Dimensional Materials. *Catal. Sci. Technol.* **2025**, *15*, 5950–5973. [CrossRef]
9. Joshi, M.; Ren, X.; Lin, T.; Joshi, R. Mechanistic Insights into Gas Adsorption on 2D Materials. *Small* **2025**, *21*, 2406706. [CrossRef]
10. Liu, X.; Zhang, Y.; Wang, C.; Shen, L. Polar Materials for Photocatalytic Applications: A Critical Review. *Interdiscip. Mater.* **2024**, *3*, 530–564. [CrossRef]
11. Pawar, K.K.; Kumar, A.; Mirzaei, A.; Kumar, M.; Kim, H.W.; Kim, S.S. 2D Nanomaterials for Realization of Flexible and Wearable Gas Sensors: A Review. *Chemosphere* **2024**, *352*, 141234. [CrossRef] [PubMed]
12. Wu, P.; Li, Y.; Yang, A.; Tan, X.; Chu, J.; Zhang, Y.; Yan, Y.; Tang, J.; Yuan, H.; Zhang, X.; et al. Advances in 2D Materials Based Gas Sensors for Industrial Machine Olfactory Applications. *ACS Sens.* **2024**, *9*, 2728–2776. [CrossRef] [PubMed]
13. Tian, X.; Wang, S.; Li, H.; Li, M.; Chen, T.; Xiao, X.; Wang, Y. Recent Advances in MoS_2-Based Nanomaterial Sensors for Room-Temperature Gas Detection: A Review. *Sens. Diagn.* **2023**, *2*, 361–381. [CrossRef]
14. Hou, W.; Mi, H.; Peng, R.; Peng, S.; Zeng, W.; Zhou, Q. First-Principle Insight into Ga-Doped MoS_2 for Sensing SO_2, SOF_2 and SO_2F_2. *Nanomaterials* **2021**, *11*, 314. [CrossRef]
15. Kumar, S.; Meng, G.; Mishra, P.; Tripathi, N.; Bannov, A.G. A Systematic Review on 2D MoS_2 for Nitrogen Dioxide (NO_2) Sensing at Room Temperature. *Mater. Today Commun.* **2023**, *34*, 105045. [CrossRef]
16. Agrawal, A.V.; Kumar, N.; Kumar, M. Strategy and Future Prospects to Develop Room-Temperature-Recoverable NO_2 Gas Sensor Based on Two-Dimensional Molybdenum Disulfide. *Nano Micro Lett.* **2021**, *13*, 38. [CrossRef]
17. Zheng, W.; Xu, Y.; Zheng, L.; Yang, C.; Pinna, N.; Liu, X.; Zhang, J. MoS_2 van Der Waals p-n Junctions Enabling Highly Selective Room-Temperature NO_2 Sensor. *Adv. Funct. Mater.* **2020**, *30*, 2000435. [CrossRef]
18. Kumar, R.; Zheng, W.; Liu, X.; Zhang, J.; Kumar, M. MoS_2-Based Nanomaterials for Room-Temperature Gas Sensors. *Adv. Mater. Technol.* **2020**, *5*, 1901062. [CrossRef]
19. Pham, T.; Li, G.; Bekyarova, E.; Itkis, M.E.; Mulchandani, A. MoS_2-Based Optoelectronic Gas Sensor with Sub-Parts-per-Billion Limit of NO_2 Gas Detection. *ACS Nano* **2019**, *13*, 3196–3205. [CrossRef]
20. Lau, T.H.M.; Lu, X.; Kulhavý, J.; Wu, S.; Lu, L.; Wu, T.-S.; Kato, R.; Foord, J.S.; Soo, Y.-L.; Suenaga, K.; et al. Transition Metal Atom Doping of the Basal Plane of MoS_2 Monolayer Nanosheets for Electrochemical Hydrogen Evolution. *Chem. Sci.* **2018**, *9*, 4769–4776. [CrossRef]
21. Kumar, R.; Goel, N.; Kumar, M. High Performance NO_2 Sensor Using MoS_2 Nanowires Network. *Appl. Phys. Lett.* **2018**, *112*, 53502. [CrossRef]
22. Ma, Y.; Zhang, D.; Ding, Z.; Ma, K. Strain-Tunable Gas Sensing Properties of Ag- and Au-Doped $SnSe_2$ Monolayers for the Detection of NO, NO_2, SO_2, H_2S and HCN. *Nanomaterials* **2025**, *15*, 1454. [CrossRef] [PubMed]
23. Cho, B.; Hahm, M.G.; Choi, M.; Yoon, J.; Kim, A.R.; Lee, Y.-J.; Park, S.-G.; Kwon, J.-D.; Kim, C.S.; Song, M.; et al. Charge-Transfer-Based Gas Sensing Using Atomic-Layer MoS_2. *Sci. Rep.* **2015**, *5*, 8052. [CrossRef] [PubMed]
24. Scardamaglia, M.; Casanova-Cháfer, J.; Temperton, R.; Annanouch, F.E.; Mohammadpour, A.; Malandra, G.; Das, A.; Alagh, A.; Arbouch, I.; Montoisy, L.; et al. Operando Investigation of WS_2 Gas Sensors: Simultaneous Ambient Pressure X-ray Photoelectron Spectroscopy and Electrical Characterization in Unveiling Sensing Mechanisms during Toxic Gas Exposure. *ACS Sens.* **2024**, *9*, 4079–4088. [CrossRef]

25. Zhang, M.; Zhu, Y.; Wang, X.; Feng, Q.; Qiao, S.; Wen, W.; Chen, Y.; Cui, M.; Zhang, J.; Cai, C.; et al. Controlled Synthesis of ZrS_2 Monolayer and Few Layers on Hexagonal Boron Nitride. *J. Am. Chem. Soc.* **2015**, *137*, 7051–7054. [CrossRef]
26. Zeng, Z.; Yin, Z.; Huang, X.; Li, H.; He, Q.; Lu, G.; Boey, F.; Zhang, H. High-Yield Preparation of Single- and Few-Layer Transition Metal Dichalcogenides by Electrochemical Lithium Intercalation and Exfoliation. *Angew. Chem. Int. Ed.* **2011**, *50*, 11093–11097. [CrossRef]
27. Tian, Y.; Li, W.; Zhou, J.; Chen, X.; Zhang, H.; Xie, L.; Li, S.; Wang, C. Epitaxial Growth of Large-Area ZrS_2 Thin Films on Sapphire for High-Performance Photodetectors. *Nano Res.* **2022**, *15*, 5678–5686. [CrossRef]
28. Turcicova, H.; Novak, O.; Muzik, J.; Stepankova, D.; Smrz, M.; Mocek, T. Laser Induced Damage Threshold (LIDT) of β-Barium Borate (BBO) and Cesium Lithium Borate (CLBO)—Overview. *Opt. Laser Technol.* **2022**, *149*, 107876. [CrossRef]
29. Ma, J.; Li, S.; Huang, X.; Jiang, J.; Xu, T.; Liu, T. All Optic-Fiber Waveguide-Coupled SPR Sensor for CRP Sensing Based on Dielectric Layer and Poly-Dopamine. *Photonic Sens.* **2025**, *15*, 250224. [CrossRef]
30. Wang, N.; Zhang, G.; Wang, G.; Feng, Z.; Li, Q.; Zhang, H.; Li, Y.; Liu, C. Pressure-induced Enhancement and Retainability of Optoelectronic Properties in Layered Zirconium Disulfide. *Small* **2024**, *20*, 2400216. [CrossRef]
31. Li, L.; Lv, R.; Wang, J.; Chen, Z.; Wang, H.; Liu, S.; Ren, W.; Liu, W.; Wang, Y. Optical Nonlinearity of ZrS_2 and Applications in Fiber Laser. *Nanomaterials* **2019**, *9*, 315. [CrossRef] [PubMed]
32. Lei, G.; Pan, H.; Mei, H.; Liu, X.; Lu, G.; Lou, C.; Li, Z.; Zhang, J. Emerging Single Atom Catalysts in Gas Sensors. *Chem. Soc. Rev.* **2022**, *51*, 7260–7280. [CrossRef] [PubMed]
33. Chu, T.; Rong, C.; Zhou, L.; Mao, X.; Zhang, B.; Xuan, F. Progress and Perspectives of Single-Atom Catalysts for Gas Sensing. *Adv. Mater.* **2023**, *35*, 2206783. [CrossRef] [PubMed]
34. Wang, X.; Zhang, Y.; Wu, J.; Zhang, Z.; Liao, Q.; Kang, Z.; Zhang, Y. Single-Atom Engineering to Ignite 2D Transition Metal Dichalcogenide Based Catalysis: Fundamentals, Progress, and Beyond. *Chem. Rev.* **2022**, *122*, 1273–1348. [CrossRef]
35. Yong, Y.; Gao, R.; Yuan, X.; Zhao, Z.; Hu, S.; Kuang, Y. Gas Sensing and Capturing Based on the C_7N_6 Monolayer with and without Metal Decoration: A First-Principles Investigation. *Appl. Surf. Sci.* **2022**, *591*, 153129. [CrossRef]
36. Liu, K.; Lin, L.; Wang, Y. Adsorption and Sensing Properties of $ZrSe_2$ Monolayer Decorated with Transition Metal for CO_2, NO_2 and SO_2 Gases: First-Principles Calculations. *Mater. Today Commun.* **2023**, *36*, 106698. [CrossRef]
37. Zhang, B.; Liu, K.; Xie, K.; Wang, P.; Lin, L.; Su, L. Adsorption of Toxic and Harmful Gas NO_2 and SO_2 on TM (Fe, Co and Ni) Decorated $ZrSe_2$ Monolayer: A DFT Study. *Mater. Today Commun.* **2024**, *39*, 108483. [CrossRef]
38. Wu, Y.-Y.; Li, W.; Ren, Q.-Y.; Li, J.-Z.; Xu, W.; Xu, J. First-Principles Study on Adsorption of Gas Molecules by Metal Sc Modified Ti_2CO_2. *Acta Phys. Sin.* **2024**, *73*, 73101. [CrossRef]
39. Zhang, J.; Zhu, X.; Zhu, K.; Shen, J.; Xu, Y.; Chen, D.; Wang, P. Adsorption of NO_2 and NH_3 on Single-Atom (Co, Pd, Pt)-Decorated 2H-MoS_2 Monolayer: A DFT Study. *Results Phys.* **2023**, *51*, 106694. [CrossRef]
40. Liu, Y.; Liu, J.; Wei, Z.; Yuan, T.; Cui, H. Single Ni Atom-Dispersed WSe_2 Monolayer for Sensing Typical Fault Gases in Dry-Type Transformers: A First-Principles Study. *ACS Omega* **2023**, *8*, 47067–47074. [CrossRef]
41. Liu, K.; Lin, L.; Xie, K.; Shi, P.; Xu, D. Adsorption and Gas-Sensing Performance of the Small-Molecule Gas on $ZrSe_2$ Monolayers: A First-Principles Study. *Langmuir* **2023**, *39*, 8879–8888. [CrossRef] [PubMed]
42. Wang, Z.; Wang, D.; Xie, K.; Shi, P.; Shen, Y.; Lin, L. Theoretical Calculation of Dissolved Gas in Transformer Oil Using the Gas Sensitive Properties of Sc- and Ti-Modified ZrS_2. *Langmuir* **2024**, *40*, 24576–24584. [CrossRef] [PubMed]
43. Tan, S.; Bi, M.; Lei, S.; He, X.; Hu, X.; He, J.; Jiang, T. Adsorption of SF_6 Decomposition Gases (H_2S, SO_2 and SOF_2) on TM (Pd and Pt) Modified Monolayer ZrS_2: A DFT Study. *Comput. Theor. Chem.* **2024**, *1236*, 114586. [CrossRef]
44. Lin, X.-Q.; Zhang, X.; Qin, Y.-Y.; Yao, Y.-G. Tuning the Gas Sensing Properties of ZrS_2 Monolayers via Pt Decoration: Insights from DFT Simulations. *Langmuir* **2025**, *41*, 6801–6815. [CrossRef]
45. Guang, Q.; Huang, B.; Li, X. Au-Decorated WS_2 Microflakes Based Sensors for Selective Ammonia Detection at Room Temperature. *Chemosensors* **2022**, *10*, 9. [CrossRef]
46. Park, J.; Mun, J.; Shin, J.-S.; Kang, S.-W. Highly Sensitive Two-Dimensional MoS_2 Gas Sensor Decorated with Pt Nanoparticles. *R. Soc. Open Sci.* **2018**, *5*, 181462. [CrossRef]
47. Zhang, L.; Huang, Z.; Xia, S. Sc-Doped Sulfur Vacancy MoS_2 Photocatalytic Nitrogen Reduction to Ammonia: Experimental and Theoretical Investigation. *Inorg. Chem.* **2025**, *64*, 15736–15747. [CrossRef]
48. Ma, Z.; Ren, C.; Wu, Y.; Qiu, H.; Liu, H.; Hu, Z.; Wu, Y. Dopant-induced Giant Photoluminescence of Monolayer MoS_2 by Chemical Vapor Transport. *Adv. Mater. Interfaces* **2022**, *9*, 2200431. [CrossRef]
49. Sahoo, K.R.; Guha, A.; Bawari, S.; Sharma, R.; Maity, D.; Narayanan, T.N. Basal Plane Activation of MoS_2 by the Substitutional Doping of Vanadium toward Electrocatalytic Hydrogen Generation. *ACS Appl. Energy Mater.* **2022**, *5*, 11263–11270. [CrossRef]
50. Kohn, W.; Sham, L.J. Self-Consistent Equations Including Exchange and Correlation Effects. *Phys. Rev.* **1965**, *140*, A1133–A1138. [CrossRef]
51. Kresse, G.; Furthmüller, J. Efficient Iterative Schemes for Ab Initio Total-Energy Calculations Using a Plane-Wave Basis Set. *Phys. Rev. B* **1996**, *54*, 11169–11186. [CrossRef]

52. Kresse, G.; Furthmüller, J. Efficiency of Ab-Initio Total Energy Calculations for Metals and Semiconductors Using a Plane-Wave Basis Set. *Comput. Mater. Sci.* **1996**, *6*, 15–50. [CrossRef]
53. Zhang, Y.; Pan, W.; Yang, W. Describing van Der Waals Interaction in Diatomic Molecules with Generalized Gradient Approximations: The Role of the Exchange Functional. *J. Chem. Phys.* **1997**, *107*, 7921–7925. [CrossRef]
54. Kresse, G.; Joubert, D. From Ultrasoft Pseudopotentials to the Projector Augmented-Wave Method. *Phys. Rev. B* **1999**, *59*, 1758–1775. [CrossRef]
55. Blöchl, P.E. Projector Augmented-Wave Method. *Phys. Rev. B* **1994**, *50*, 17953–17979. [CrossRef]
56. Grimme, S.; Antony, J.; Ehrlich, S.; Krieg, H. A Consistent and Accurate Ab Initio Parametrization of Density Functional Dispersion Correction (DFT-D) for the 94 Elements H-Pu. *J. Chem. Phys.* **2010**, *132*, 154104. [CrossRef]
57. Monkhorst, H.J.; Pack, J.D. Special Points for Brillouin-Zone Integrations. *Phys. Rev. B* **1976**, *13*, 5188–5192. [CrossRef]
58. Lau, K.W.; Cocchi, C.; Draxl, C. Electronic and Optical Excitations of Two-Dimensional ZrS_2 and HfS_2 and Their Heterostructure. *Phys. Rev. Mater.* **2019**, *3*, 74001. [CrossRef]
59. Li, Y.; Kang, J.; Li, J. Indirect-to-Direct Band Gap Transition of the ZrS_2 Monolayer by Strain: First-Principles Calculations. *RSC Adv.* **2014**, *4*, 7396. [CrossRef]
60. Wang, V.; Xu, N.; Liu, J.-C.; Tang, G.; Geng, W.-T. VASPKIT: A User-Friendly Interface Facilitating High-Throughput Computing and Analysis Using VASP Code. *Comput. Phys. Commun.* **2021**, *267*, 108033. [CrossRef]
61. Momma, K.; Izumi, F. VESTA 3 for Three-Dimensional Visualization of Crystal, Volumetric and Morphology Data. *J. Appl. Crystallogr.* **2011**, *44*, 1272–1276. [CrossRef]
62. Maintz, S.; Deringer, V.L.; Tchougréeff, A.L.; Dronskowski, R. LOBSTER: A Tool to Extract Chemical Bonding from Plane-wave Based DFT. *J. Comput. Chem.* **2016**, *37*, 1030–1035. [CrossRef]
63. Dronskowski, R.; Bloechl, P.E. Crystal Orbital Hamilton Populations (COHP): Energy-Resolved Visualization of Chemical Bonding in Solids Based on Density-Functional Calculations. *J. Phys. Chem.* **1993**, *97*, 8617–8624. [CrossRef]
64. Bader, R.F.W. *Atoms in Molecules: A Quantum Theory*; Clarendon Press: Oxford, UK, 1994.
65. Tang, W.; Sanville, E.; Henkelman, G. A grid-based Bader analysis algorithm without lattice bias. *J. Phys. Condens. Matter* **2009**, *21*, 084204. [CrossRef] [PubMed]
66. Sanville, E.; Kenny, S.D.; Smith, R.; Henkelman, G. An Improved Grid-Based Algorithm for Bader Charge Allocation. *J. Comput. Chem.* **2007**, *28*, 899–908. [CrossRef] [PubMed]
67. Henkelman, G.; Arnaldsson, A.; Jónsson, H. A Fast and Robust Algorithm for Bader Decomposition of Charge Density. *Comput. Mater. Sci.* **2006**, *36*, 254–360. [CrossRef]
68. Becke, A.D.; Edgecombe, K.E. A Simple Measure of Electron Localization in Atomic and Molecular Systems. *J. Chem. Phys.* **1990**, *92*, 5397–5403. [CrossRef]
69. Silvi, B.; Savin, A. Classification of Chemical Bonds Based on Topological Analysis of Electron Localization Functions. *Nature* **1994**, *371*, 683–686. [CrossRef]
70. Kühne, T.D.; Iannuzzi, M.; Del Ben, M.; Rybkin, V.V.; Seewald, P.; Stein, F.; Laino, T.; Khaliullin, R.Z.; Schütt, O.; Schiffmann, F.; et al. CP2K: An Electronic Structure and Molecular Dynamics Software Package—Quickstep: Efficient and Accurate Electronic Structure Calculations. *J. Chem. Phys.* **2020**, *152*, 194103. [CrossRef]
71. Lu, T. A Comprehensive Electron Wavefunction Analysis Toolbox for Chemists, Multiwfn. *J. Chem. Phys.* **2024**, *161*, 82503. [CrossRef]
72. Lu, T.; Chen, F. Multiwfn: A Multifunctional Wavefunction Analyzer. *J. Comput. Chem.* **2012**, *33*, 580–592. [CrossRef] [PubMed]
73. Karbalaee Aghaee, A.; Belbasi, S.; Hadipour, H. Ab Initio Calculation of the Effective Coulomb Interactions in MX_2 (M = Ti, V, Cr, Mn, Fe, Co, Ni; X = S, Se, Te): Intrinsic Magnetic Ordering and Mott Phase. *Phys. Rev. B* **2022**, *105*, 115115. [CrossRef]
74. Hu, T.; Li, Z.; Hu, M.; Wang, J.; Hu, Q.; Li, Q.; Wang, X. Chemical Origin of Termination-Functionalized MXenes: $Ti_3C_2T_2$ as a Case Study. *J. Phys. Chem. C* **2017**, *121*, 19254–19261. [CrossRef]
75. Yi, W.; Tang, G.; Chen, X.; Yang, B.; Liu, X. Qvasp: A Flexible Toolkit for VASP Users in Materials Simulations. *Comput. Phys. Commun.* **2020**, *257*, 107535. [CrossRef]
76. Han, Y. An Evaluation for Geometries, Formation Enthalpies, and Dissociation Energies of Diatomic and Triatomic (C, H, N, O), NO_3, and HNO_3 Molecules from the PAW DFT Method with PBE and optB88-vdW Functionals. *AIP Adv.* **2022**, *12*, 120501. [CrossRef]
77. Zhu, M.-Q.; Wang, X.-F.; Vasilopoulos, P. Transition Metal-Doped ZrS_2 Monolayer as Potential Gas Sensor for CO_2, SO_2, and NO_2: Density Functional Theory and Non-Equilibrium Green's Functions Analysis. *J. Phys. D Appl. Phys.* **2025**, *58*, 135306. [CrossRef]
78. Xin, Q.; Zhao, X.; Ma, X.; Wu, N.; Liu, X.; Wei, S. Electronic Structure in 1T-ZrS_2 Monolayer by Strain. *Phys. E Low-Dimens. Syst. Nanostructures* **2017**, *93*, 87–91. [CrossRef]
79. Zhao, X.; Zhang, X.; Wang, T.; Wei, S.; Yang, L. Electronic Structures and Optical Properties of ZrS_2 Monolayer by N- and P-Type Doping. *J. Alloys Compd.* **2018**, *748*, 798–803. [CrossRef]

80. Raya, S.S.; Ansari, A.S.; Shong, B. Molecular Adsorption of NH_3 and NO_2 on Zr and Hf Dichalcogenides (S, Se, Te) Monolayers: A Density Functional Theory Study. *Nanomaterials* **2020**, *10*, 1215. [CrossRef]
81. Chen, Y.; Gui, Y.; Chen, X. Adsorption and Gas-Sensing Properties of C_2H_4, CH_4, H_2, H_2O on Metal Oxides (CuO, NiO) Modified SnS_2 Monolayer: A DFT Study. *Results Phys.* **2021**, *28*, 104680. [CrossRef]
82. Zhang, Y.-H.; Chen, Y.-B.; Zhou, K.-G.; Liu, C.-H.; Zeng, J.; Zhang, H.-L.; Peng, Y. Improving Gas Sensing Properties of Graphene by Introducing Dopants and Defects: A First-Principles Study. *Nanotechnology* **2009**, *20*, 185504. [CrossRef]
83. Peng, S.; Cho, K.; Qi, P.; Dai, H. Ab Initio Study of CNT NO_2 Gas Sensor. *Chem. Phys. Lett.* **2004**, *387*, 271–276. [CrossRef]
84. Guo, C.; Wang, Z.; Wang, D.; Wang, H.-F.; Hu, P. First-Principles Determination of CO Adsorption and Desorption on Pt (111) in the Free Energy Landscape. *J. Phys. Chem. C* **2018**, *122*, 21478–21483. [CrossRef]

Disclaimer/Publisher's Note: The statements, opinions and data contained in all publications are solely those of the individual author(s) and contributor(s) and not of MDPI and/or the editor(s). MDPI and/or the editor(s) disclaim responsibility for any injury to people or property resulting from any ideas, methods, instructions or products referred to in the content.